Iraqi Journal of Physics, 2026 *Vol.24, No.3, PP.137-146*
https://doi.org/10.30723/ijp.v24i3.2026 *P-ISSN: 2070-4003*
E-ISSN: 2664-5548

Structural Properties of $CoFe_2O_4$ and $CoFe_{1.6}Mo_{0.4}O_4$ Prepared by Chemical Method

Sura S. Mahdee[1*] and Nathera A. Ali[1]
[1]*Department of Physics, College of Science, University of Baghdad, Baghdad, Iraq*
[*]Corresponding author: sura.salah1984@gmail.com

Abstract
The current study examined the structural characteristics of two spinel ferrite materials: cobalt ferrite ($CoFe_2O_4$) and molybdenum-doped cobalt ferrite ($CoFe_{2-x}Mo_xO_4$) (CMFO) with x=0.4. The chemical method successfully created magnetic nanoparticles of $CoFe_2O_4$ and $CoFe_{1.6}Mo_{0.4}O_4$. Atomic force microscopy (AFM), X-ray diffraction (XRD), field emission scanning electron microscopy (FESEM), and energy-dispersive X-ray spectroscopy (EDX) were used for the structural and morphological characterization. XRD patterns confirmed the presence of cubic phases in the composites. Furthermore, the XRD results indicated that the nanoparticles' structures displayed a mixed phase of $CoFe_2O_4$ and $CoFe_{1.6}Mo_{0.4}O_4$, with an average crystalline size ranging from 15.166 to 19.638 nm, including the effect of Mo. According to FESEM images, the produced ferrite particles were aggregated and fairly round. The $CoFe_2O_4$ image showed diameters between 67 and 277 nm, whereas the $CoFe_{1.6}Mo_{0.4}O_4$ image showed diameters between 59 and 360 nm. There was an emission line for oxygen (O) and emission lines for metals (Fe, Mo, and Co) in the EDX spectra. AFM was used for the surface topography investigation. Nanostructures with average sizes ranging from 123.4 to 94.7 nm were evenly distributed in the AFM images.

Article Info.

Keywords:
Chemical Method, Magnetic Materials, Nanoparticles, Ferrite, Structural Properties.

Article history:
Received: Oct. 08, 2024
Revised: Mar. 12, 2025
Accepted:Apr. 18, 2025
Published:Sep. 01,2026

1. Introduction
Spinel ferrites have the general chemical formula of MFe_2O_4, where M represents divalent ions, commonly known as Fe^{2+}, Mg^{2+}, Co^{2+}, Ni^{2+}, Zn^{2+}, and Mn^{2+}. The structural characteristics of ferrites doped with cobalt ($CoFe_{2-x}Mo_xO_4$) (where x = 0, 0.4) were examined in this research. Spinel ferrites are a significant family of magnetic materials that have been the subject of substantial research in the last several decades due to their possible uses in spintronics, microwave devices, magnetic storage, magnetic refrigeration, biomedicine, environmental remediation, catalysis, and other related domains [1, 2]. The distribution and type of cations on the tetrahedral (A) and octahedral (B) sublattices of a generic AB_2O_4 spinel structure strongly determine the electrical and magnetic characteristics of these materials [3]. Several synthetic techniques and tactics for doping different metal cations at either A or B cation sites have been developed in response to the large-scale uses of ferrites and the possibilities for modifying their magnetic and electrical characteristics [4]. A significant change in magnetic entropy was observed due to the demagnetization process, which reflects alterations in the material's spin configuration [5, 6]. This system was selected assuming that electron doping should be induced by partially replacing Fe^{3+} ions with Mo^{6+} ions in $CoFe_{1.6}Mo_{0.4}O_4$, increasing the concentration of Fe^{2+} ions at the tetrahedral sites. Therefore, researching how this replacement impacts the structural features of $CoFe_2O_4$ and $CoFe_{1.6}Mo_{0.4}O_4$ ferrite would be an intriguing endeavor. The purpose of this research is to learn more about using ferrite nanocomposites, such as $CoFe_2O_4$ and $CoFe_{1.6}Mo_{0.4}O_4$, to remove air and water pollutants.

2. Experimental Work
The $CoFe_2O_4$ and $CoFe_{1.6}Mo_{0.4}O_4$ nanoparticles were synthesized via a chemical co-precipitation method using cobalt (II) nitrate hexahydrate [$Co(NO_3)_2 \cdot 6H_2O$], iron (III) nitrate

nonahydrate [$Fe(NO_3)_3 \cdot 9H_2O$], and molybdenum (VI) oxide [MoO_3] as starting materials. Each compound was accurately weighed (0.5 g) and dissolved separately in deionized water, with concentrated nitric acid added as needed to facilitate the dissolution of MoO_3. The solutions were then combined in a 500 mL glass beaker and stirred magnetically for 30 minutes at room temperature. Ethanol was slowly added to the mixture at a 2:1 ethanol-to-metal salt ratio, followed by continuous stirring until a homogeneous solution was achieved. The mixture was heated on a hot plate at 60–80 °C to promote solvent evaporation until a gel-like precipitate formed. This gel was dried in an oven at 100–120°C for 12 hrs and then ground into a fine powder. The resulting material was calcined in a muffle furnace at 600–800 °C for 3–5 hrs and allowed to cool gradually inside the furnace. The final powder was reground to ensure homogeneity and stored in sealed containers to prevent contamination. Characterization techniques such as X-ray Diffraction (XRD), Scanning Electron Microscopy (SEM), Energy-Dispersive X-Ray Spectroscopy (EDX), and Atomic Force Microscopy (AFM) were employed to assess the crystalline structure, morphology, elemental composition, and surface topography of the synthesized nanoparticles.

3. Results and Discussion

3.1. Description and Analysis of the XRD Pattern

Two XRD patterns are shown in Fig.1 for the two samples of ($CoFe_{1.6}Mo_{0.4}O_4$) where x=0.4 (brown line), and $CoFe_{2-x}Mo_xO_4$, where x=0.0 (black line). The peaks in the pattern correspond to specific crystal planes, indexed by their Miller indices. Peaks for $CoFe_2O_4$ (Cobalt Ferrite) are labelled in red, while peaks for MoO_3 (Molybdenum Oxide) are labelled in green. $CoFe_2O_4$ peaks (indexed with their Miller indices) include:(111), (220),(311),(222), (400), (422), (511), (440), (620), (533), (622), (444), MoO_3 peaks include (020), (110), (040), (021).

The $CoFe_2O_4$ peaks indicate the presence of a spinel structure typical of cobalt ferrite, confirming the successful synthesis of this compound. The presence of MoO_3 peaks in the x=0.4 sample suggests the incorporation of molybdenum into the lattice, which could indicate a substitutional solid solution or secondary phase formation. The x=0.0 sample (black line) shows peaks corresponding only to $CoFe_2O_4$, confirming the pure phase of cobalt ferrite $CoFe_2O_4$ without any MoO_3. The x=0.4 sample (brown line) displays additional peaks corresponding to MoO_3, indicating the presence of molybdenum in the sample. Individual diffraction patterns consist of an amorphous halo superimposed with polycrystalline diffraction rings. This structure is characterized by identifiable diffraction peaks located at 2θ of 18.7057°, 30.4299°, 35.8705°, 37.3264°, 43.5716°, 53.8015°, 57.4414°, 63.0736°, and 74.4146°. According to the data from JCPDS card number 22–1086 [7], these values correspond to standard diffraction peaks attributed to the spinel cobalt ferrite phase. The diffracted lines associated with this phase include the crystallographic planes (111), (220), (311), (222), (400), (422), (511), (440), and (533). These lines serve as reference points for electron diffraction patterns.

The XRD pattern peaks provide crucial information about the synthesized materials' crystallographic planes and phase purity. The sharpness and intensity of the peaks suggest well-crystallized structures. The fluctuation in peak sharpness is correlated with the extent of crystallinity. Samples exhibiting sharp peaks demonstrated a more ordered arrangement than those characterized by broad peaks. The displacement in peak positions arises from structural modifications resulting from substituting iron ions with molybdenum, consequently leading to a modification in the lattice parameter and an escalation in lattice strain. This phenomenon is directly manifested in the magnetic and mechanical properties.

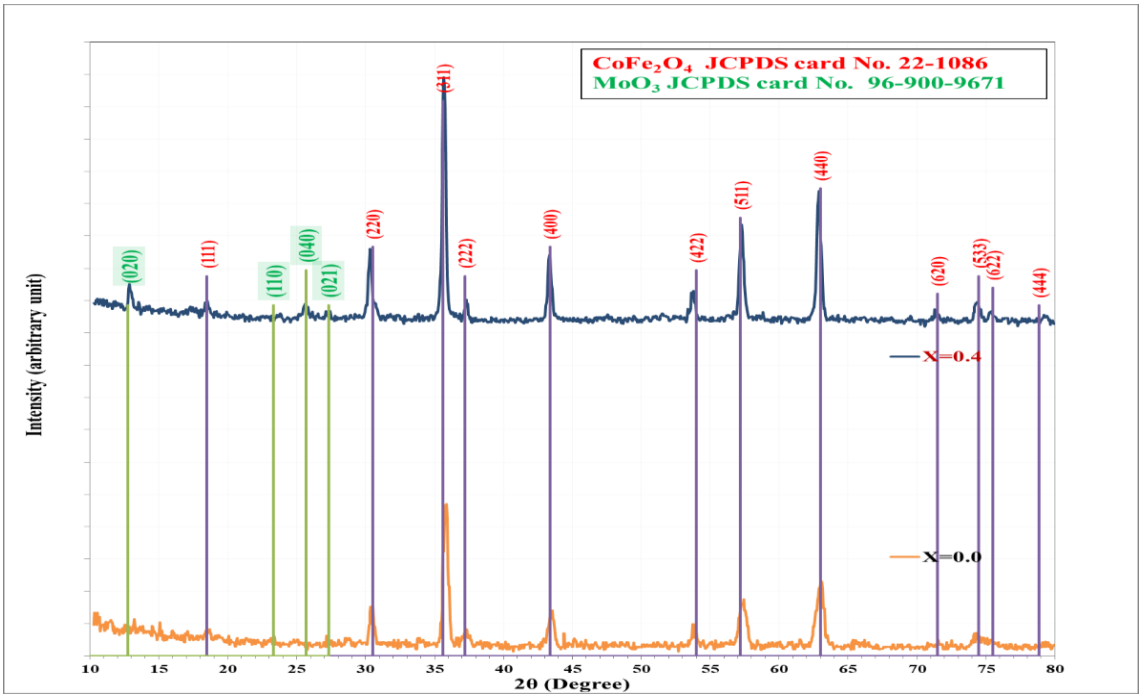

Figure 1: XRD patterns for $CoFe_2O_4$ and $CoFe_{1.6}Mo_{0.4}O_4$ powders prepared by chemical method.

By replacing Fe in $CoFe_2O_4$ with Mo, resulting in $CoFe_{1.6}Mo_{0.4}O_4$, the locations of the peaks exhibit a slight shift toward lower diffraction angles. This phenomenon illustrates the changes in the lattice parameter due to variations in the ionic radii of the constituent ions. As pointed out by Liu et al. [8], the ionic radius of Mo is 0.69 Å, whereas that of Fe is 0.64 Å. The inequality in the ionic radii leads to lattice strain within the crystal structure. Furthermore, the degree of crystallinity increases, while the broadening of the line width is only slightly affected. This result supports the conclusions obtained earlier in our work, and those presented by Liu et al. [8].

The Bragg equation was employed to determine the interplanar distances d_{hkl} within the crystal layers. The Scherrer equation was used to determine the crystallite size based on the broadening of the diffraction lines at Full Width at Half Maximum (FWHM) values [9]. All these results are comprehensively presented in Table 1.

More specifically, the Crystallite Size (C.S.) increases at a Mo ratio of 0.4. This observation is consistent with the relationship inherent in cubic structures:

$$d_{hkl} = \frac{a}{\sqrt{h^2+k^2+l^2}} \quad \textbf{(1)}$$

Fig. 2 illustrates how the slope of the straight line passing through the origin was utilized to determine the lattice constant (a) of both the $CoFe_2O_3$ and the Mo-doped samples. In this graph, the values of d_{hkl} were plotted on the vertical axis, while the values of $\frac{1}{\sqrt{h^2+k^2+l^2}}$ on the horizontal axis. The coefficient of determination (R^2) is a statistical measure of the accuracy of the linear regression, where a higher R^2 value indicates greater reliability. From Fig. 2, the R^2 value is nearly equal to 1, suggesting a highly linear relationship between the variables. As shown in Table 2, the lattice constants of the synthesized cobalt ferrite range from 8.2736 Å to 8.3401 Å. The lattice constant increased to 8.376 Å when molybdenum (Mo) was incorporated into the compound's structure. This significant rise can be attributed to lattice strain, potentially resulting from crystal defects or the presence of a secondary phase [10]. Furthermore, the lattice densities of both the Mo-doped and Co-doped samples were calculated using the Smith and

Winn formula [11]. These calculations are crucial for understanding the impact of Mo doping on the structural properties of cobalt ferrite

$$\rho_x = \frac{n\, M_w}{N_A\, a^3} \quad \textbf{(2)}$$

where N_A is the number of molecules present in the unit cell; all spinel structures contain eight molecules [12], and Mw is the molecular weight, which is the sum of the atomic weights of all elements of a compound. In computing the changes in distance between magnetic ions in the tetrahedral A-site (L_A) and the octahedral B-site (L_B) from one another, Eqs. (3 and 4) were employed [13, 14]. This was done for easy comparison between these two sites.

$$L_A = \frac{\sqrt{3}a}{4} \quad \textbf{(3)}$$

$$L_B = \frac{\sqrt{3}a}{2} \quad \textbf{(4)}$$

The lattice constant (a), lattice volume (V), lattice density (ρ), and the ion jump lengths (L_A and L_B) were successfully calculated and presented in Table 2. The ionic radii discrepancies are the reason for the sensitivity of the ion jump lengths (L_B and L_A) to the quantity of molybdenum exchanged for iron in the spinel ferrite lattice. This assumption was made based on the observed fluctuations, which support the proposed hypothesis.

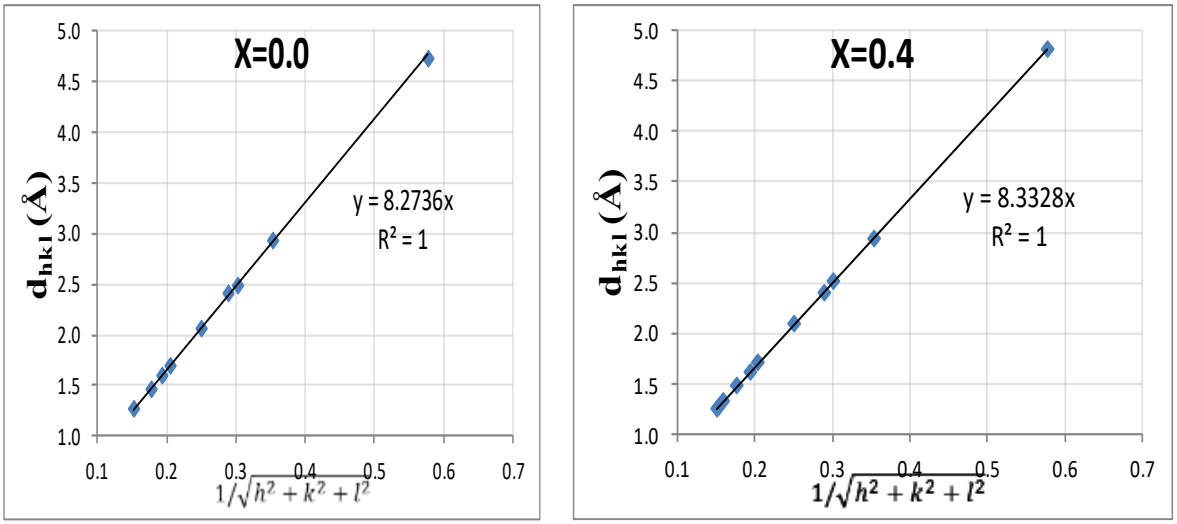

Figure 2: The relation between d_{hkl} and $\frac{1}{\sqrt{h^2+k^2+l^2}}$ for $CoFe_2O_4$ and $CoFe_{1.6}Mo_{0.4}O_4$ powders prepared by the chemical method.

Table 1: XRD parameters for $CoFe_2O_4$ and $CoFe_{1.6}Mo_{0.4}O_4$ powders prepared by chemical method.

Samples	2θ (Deg.)	FWHM (Deg.)	d_{hkl} (Å)	C.S (nm)	hkl	Phase
X=0.0	18.7057	0.5364	4.7399	15.0	(111)	$CoFe_2O_4$
	30.4299	0.4215	2.9351	19.5	(220)	$CoFe_2O_4$
	35.8705	0.4981	2.5014	16.8	(311)	$CoFe_2O_4$
	37.3264	0.6513	2.4072	12.9	(222)	$CoFe_2O_4$
	43.5716	0.5747	2.0755	14.9	(400)	$CoFe_2O_4$
	53.8015	0.4598	1.7025	19.4	(422)	$CoFe_2O_4$
	57.4414	0.6514	1.6030	13.9	(511)	$CoFe_2O_4$
	63.0736	0.7280	1.4727	12.8	(440)	$CoFe_2O_4$
	74.4146	0.8812	1.2739	11.3	(533)	$CoFe_2O_4$
X=0.4	12.9885	0.4215	6.8106	19.0	(020)	MoO_3
	18.4483	0.4406	4.8055	18.3	(111)	$CoFe_2O_4$
	25.7088	0.6130	3.4624	13.3	(040)	MoO_3
	30.3448	0.3470	2.9432	23.7	(220)	$CoFe_2O_4$
	35.7280	0.3690	2.5111	22.6	(311)	$CoFe_2O_4$
	37.3180	0.3832	2.4077	21.9	(222)	$CoFe_2O_4$
	43.3333	0.4112	2.0864	20.8	(400)	$CoFe_2O_4$
	53.7357	0.4406	1.7045	20.2	(422)	$CoFe_2O_4$
	57.3180	0.4540	1.6061	20.0	(511)	$CoFe_2O_4$
	62.9502	0.4865	1.4753	19.2	(440)	$CoFe_2O_4$
	71.3602	0.5182	1.3207	18.9	(620)	$CoFe_2O_4$
	74.3870	0.5280	1.2743	18.9	(533)	$CoFe_2O_4$
	75.3832	0.5432	1.2599	18.5	(622)	$CoFe_2O_4$

Table 2: Lattice constant (a), lattice volume (V), lattice density (ρ_x), and ion jump lengths (L_A, L_B) for $CoFe_2O_4$ and $CoFe_{1.6}Mo_{0.4}O_4$ powders prepared by the chemical method.

X	a (Å)	V(Å^3)	ρ(g/cm^3)	L_A	L_B
0	8.2736	566.348	5.504	3.583	7.165
0.4	8.3328	578.593	5.755	3.608	7.216

3.2. Field Emission Scanning Electron Microscopy (FESEM)

A detailed physical characterization of the $CoFe_2O_4$ and $CoFe_{1.6}Mo_{0.4}O_4$ powder samples was effectively accomplished using FESEM. The images obtained from this analysis are shown in Fig. 3. It was necessary to use two different magnification factors for each sample

in addition to acquiring high-resolution photographs: x25,000 and x200,000. The cobalt ferrite sample ($CoFe_2O_4$, x=0) exhibited a fairly large porosity in morphology. The nanoparticles (NPs) that constitute this design were relatively small, with nearly spherical geometries, and ranged in size from 67 to 277 nanometers, forming the fundamental structural framework [15].

It was observed that the properties of the samples changed with molybdenum. Externally, the particles were covered with very small particles, forming patterns that develop into large, irregular, multifaceted, pentahedral structures. In some ways, these structures resemble geological formations or formations of armies in a battle. Oehlerking et al. noted that the particle size of the materials formed increases with higher molybdenum concentrations [16]. The study revealed a strong relationship between the concentration of molybdenum and the surface morphology of $CoFe_{1.6}Mo_{0.4}O_4$ powder samples, highlighting its significance.

The incorporation of molybdenum into the composite leads to changes in the nucleation and growth mechanisms of the nanoparticles. These changes can be observed in the progression from porous structures to those with diminutive, spherical nanoparticles, and eventually to larger, angular polyhedra. Understanding these morphological differences is crucial for tailoring the material's features to specific applications, such as magnetic materials or catalysis [17]. This enables the material to meet the specialized needs of certain applications by improving its ability to fine-tune its properties accordingly.

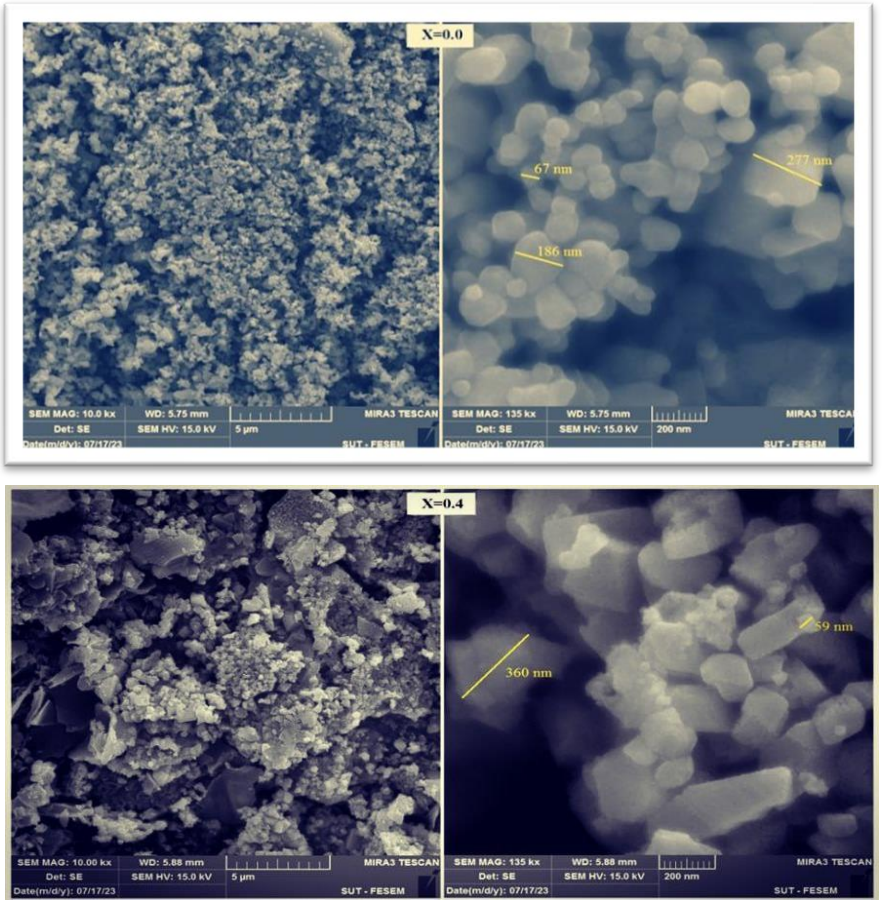

Figure 3: FESEM for $CoFe_2O_4$ and $CoFe_{1.6}Mo_{0.4}O_4$ powders prepared by chemical method.

3.3. Elemental Analysis

To obtain the proportional quantitative analysis of the samples, Energy-Dispersive X-ray Spectroscopy (EDX) was employed on nanoparticles of $CoFe_2O_3$ and $CoFe_{1.6}Mo_{0.4}O_4$. These nanoparticles were synthesized using the specified synthesis process, both with and without molybdenum. The EDX patterns showed new spectral lines derived from the emission

spectra of specific elements in the sample, as depicted in Fig. 4 [18]. The spectra revealed that $CoFe_2O_3$ nanoparticles encompassed peaks of various metallic elements, including Iron (Fe), molybdenum (Mo), cobalt (Co), and oxygen (O) [19]. Additionally, peaks corresponding to gold (Au) were present due to a thin layer of gold deposited on the sample surface to obtain high-resolution details via FESEM imaging [20, 21]. This behavior could be attributed to the different oxidation tendencies of the metals. Complete details of the EDX analysis, including information on molybdenum and other elements, are provided in Table 3.

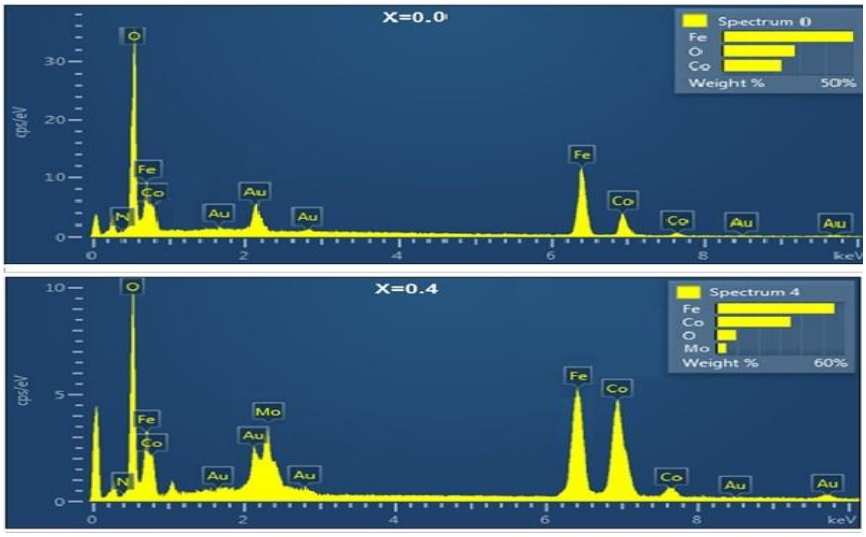

Figure 4: EDX patterns for $CoFe_2O_4$ and $CoFe_{1.6}Mo_{0.4}O_4$ powders prepared by chemical method.

Table 3: Elemental analysis for $CoFe_2O_4$ and $CoFe_{1.6}Mo_{0.4}O_4$ powders prepared by chemical method.

X	Element	Wt.%	Atomic %
0	N	0.36	1.14
	O	28.87	57.87
	Fe	48.55	28.95
	Co	22.22	12.04
0.4	N	0.47	1.295
	O	15.63	38.19
	Fe	45.94	35.195
	Mo	6	3
	Co	31.96	22.32

3.4. Atomic Force Microscopy (AFM)

Atomic Force Microscopy (AFM) was utilized to analyze the synthesized nanoparticles to establish specific details of their surface morphology. Fig. 5 presents three-dimensional AFM images and the respective particle size distribution histograms, which indicate significant changes in surface topographical characteristics with the introduction of molybdenum [22]. For the sample with x=0, the AFM image revealed uniformly deposited particles on the surface [23]. The average diameter of these nanoparticles was 123.4 nm, indicating that the size distribution is fairly monodisperse. The actual low surface roughness of 8.7 nm depicts a relatively smooth surface texture [24].

The presence of Mo (in the x=0.4 sample) resulted in a decrease in the average particle diameter to 94.7 nm. This reduction may be attributed to the influence of Mo on the nucleation and growth processes during nanoparticle formation. However, a decrease in surface roughness at this Mo ratio was recorded, indicating a transition from a smoother to a more rugged surface [25,26]. At this Mo ratio, the particle size distribution is split into two distinct modes [27, 28, 29]. Based on data analysis, the log-normal (LOGN) distribution profile observed here exhibits a hysteresis-like behavior, indicating the presence of two distinct nanoparticle populations with different size ranges. This bimodal distribution is likely attributed to variations in synthesis parameters or the emergence of multiple crystalline phases during the formation process.

Understanding these morphological differences is essential for tailoring the material's properties to specific applications, such as in magnetic materials or catalysis. The alterations in surface roughness and the distribution of grain morphology, as evidenced by AFM analyses, significantly influence the efficacy of both magnetic and catalytic applications. For instance, in the context of magnetic applications involving $CoFe_{1.6}Mo_{0.4}O_4$, a decrease in grain size leads to an augmentation of the effective surface area, thereby enhancing the operational capabilities of the material in magnetic storage systems. In catalytic contexts, a uniform distribution of particle sizes, coupled with increased pore volume, significantly improves the catalytic efficiency of chemical reactions, rendering it advantageous for applications aimed at facilitating the oxidation of pollutants present in both aqueous and atmospheric environments. Table 4 shows AFM results for $CoFe_2O_4$ and $CoFe_{1.6}Mo_{0.4}O_4$ powders prepared by the chemical method.

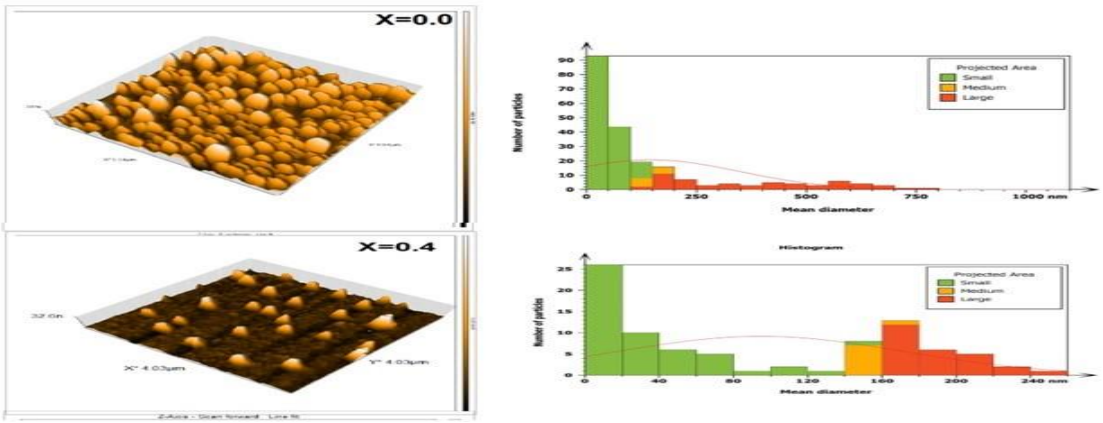

Figure 5: AFM and particle size distribution for $CoFe_2O_4$ and $CoFe_{1.6}Mo_{0.4}O_4$ powders prepared by the chemical method.

Table 4: AFM results for $CoFe_2O_4$ and $CoFe_{1.6}Mo_{0.4}O_4$ powders prepared by chemical method.

X	Average Diameter (nm)	RMS Roughness (nm)
0.0	123.4	8.7
0.4	94.7	8.1

4. Conclusions

The chemical synthesis of iron nitrate and cobalt in the presence of ammonium molybdate exhibited a direct correlation between the molybdenum concentration (x value) and particle size, with larger particles corresponding to higher x values. This study specifically examined the structural modifications induced by molybdenum substitution in the synthesized nanoparticles. Findings indicate that an increased ratio of ammonium molybdate to iron nitrate

during synthesis significantly enhanced water purification efficiency. This improvement is likely attributed to alterations in nanoparticle surface properties and enhanced catalytic activity. Additionally, the incorporation of molybdenum into the lattice structure improved oxidation resistance, contributing to the stability and functionality of the nanoparticles in purification processes. The ability of molybdenum-modified nanoparticles to interact more effectively with contaminants suggests their potential for optimizing water treatment methodologies. These results underscore the importance of fine-tuning the molybdenum-to-iron ratio in nanoparticle synthesis to achieve superior yields for biomedical applications.

Conflict of Interest

The authors declare that they have no conflict of interest.

References

1. S. Salah and N. A. Al-Tememee, Studying the effect of adding Mo on the optical and structural properties of the $CoFe_2O_4$ compound, *J. Optics*, **53**(4), 3956 (2024). https://doi.org/10.1007/s12596-023-01577-0.
2. V. Tsurkan, H. A. K. Von Nidda, J. Deisenhofer, P. Lunkenheimer, and A. Loidl, On the complexity of spinels: Magnetic, electronic, and polar ground states, *Phys. Rep.* **926**, 1 (2021). https://doi.org/10.1016/j.physrep.2021.04.002.
3. S. J. Salih and W. M. Mahmood, Review on magnetic spinel ferrite (MFe_2O_4) nanoparticles: From synthesis to application, *Heliyon*. **9(**6), e16601 (2023). https://doi.org/10.1016/j.heliyon.2023.e16601.
4. Q. F. Xu, M. T. Chen, R. T. Wu, L. S. Long, and L. S. Zheng. Achieving magnetic refrigerants with large magnetic entropy changes and low magnetic ordering temperatures, *J. Am. Chem. Soc.* **124**(29), 20116 (2024). https://doi.org/10.1021/jacs.4c04258.
5. B. T. Chiad, M. T. Al-Helaly, M. S. Essa, and N. A. Al-Tememee, Effect of red laser irradiation on the optical properties of cobalt oxide (CoO_2) thin films deposited via semi-computerized spraying technique, *J. Phys: Conf. Ser.* **1897**(1), 012066 (2021). https://doi.org/10.1088/1742-6596/1897/1/012066.
6. J. L. Ortiz-Quiñonez, U. Pal, and M. S. Villanueva, Structural, magnetic, and catalytic evaluation of spinel Co, Ni, and Co–Ni ferrite nanoparticles fabricated by low-temperature solution combustion process, *ACS Omega.* **3**(11), 14986 (2018). https://doi.org/10.1021/acsomega.8b02229.
7. I. Ibrahim, I. O. Ali, T. M. Salama, A. A. Bahgat, M. M. Mohamed, Synthesis of magnetically recyclable spinel ferrite (MFe_2O_4, M = Zn, Co, Mn) nanocrystals engineered by sol gel-hydrothermal technology: High catalytic performances for nitroarenes reduction, *Appl. Catal. B.* 181, 389 (2016).
8. Y. Liu, Y. Liu, and M. G. B. Drew, Comparison of calculations for interplanar distances in a crystal lattice, *Crystallogr. Rev.* **23**(4), 252 (2017). https://doi.org/10.1080/0889311X.2017.1323332.
9. B. Jeevanantham, Y. Song, H. Choe, and M. K. Shobana, Structural and optical characteristics of cobalt ferrite nanoparticles, *Mater. Lett. X*, **12**, 100105 (2021). https://doi.org/10.1016/j.mlblux.2021.100105.
10. F. Sharifianjazi et al. Magnetic $CoFe_2O_4$ nanoparticles doped with metal ions: A review, *Ceram. Int.* **46**(11), 18391 (2020). https://doi.org/10.1016/j.ceramint.2020.04.202.
11. T. Tatarchuk, M. Bououdina, J. J. Vijaya, and L. J. Kennedy, Spinel ferrite nanoparticles: synthesis, crystal structure, properties, and perspective applications, Nanophysics, Nanomaterials, Interface Studies, and Applications, Springer Nature, **195**, (2017). https://doi.org/10.1007/978-3-319-56422-7_22.
12. A. R. Chavan, R. R. Chilwar, P. B. Kharat, and K. M. Jadhav, Effect of annealing temperature on structural, morphological, optical and magnetic properties of $NiFe_2O_4$ thin films, *Supercond. Nov. Mag.* **31**, 2949 (2018). https://doi.org/10.1007/s10948-018-4565-3.
13. R. Tiwaria, M. De, H. S. Tewari, and S. K. Ghoshal, Structural and magnetic properties of tailored $NiFe_2O_4$ nanostructures synthesized using auto-combustion method, *RESULTS PHYSICS*. **16**, 102916 (2020). https://doi.org/10.1016/j.rinp.2019.102916.
14. A. Khan, K. Balakrishnan, and A. Z. M. S. Rahman, ZnO/ZnMgO: cubic quantum well laser in UV spectrum, *Int J Adv Manuf Technol.* **89**, 629 (2016). https://doi.org/10.1016/B978-0-12-803581-8.00828-6.
15. N. A. A. AL-Tememee, Preparation of nano-microfibers with a different polymers, *Iraqi J. Phys.* **9**(15), 68 (2011).
16. F. Oehlerking, M. T. Stawovy, S. Ohm, and A. Imandoust, Microstructural characterization and mechanical properties of additively manufactured molybdenum and molybdenum alloys, *Int. J. Refract. Met. Hard Mater*. **109**, 105971 (2022). https://doi.org/10.1016/j.ijrmhm.2022.105971.
17. D. Rehnlund, C. Ihrfors, J. Maibach, and L. Nyholm, Dendrite-free lithium electrode cycling via controlled nucleation in low $LiPF_6$ concentration electrolytes, *Mater. Today*, **21**(10), 1010 (2018). https://doi.org/10.1016/j.mattod.2018.08.003.

18. P. P. Hankare, U. B. Sankpal, R. P. Patil, I. S. Mulla, P. D. Lokhande, and N. S. Gajbhiye, Synthesis and characterization of $CoCr_xFe_{2-x}O_4$ nanoparticles, *J. Alloys Compd.* **485**(1–2), 798 (2009). https://doi.org/10.1016/j.jallcom.2009.06.087.
19. K. Jalaiah, K. C. Mouli, K. V. Babu, and R. V. Krishnaiah, Structural, electrical and magnetic properties of Mg-Zr co-substituted $Ni_{0.5}Zn_{0.5}Fe_2O_4$, *J. Sci.: Adv. Mater. Devices*. **4**(2), 310 (2019). https://doi.org/10.1016/j.jsamd.2018.12.004.
20. M. Abd Mutalib, M. A. Rahman, M. H. D. Othman, A. F. Ismail, and J. Jaafar, Chapter 9 - Scanning Electron Microscopy (SEM) and Energy-Dispersive X-Ray (EDX) Spectroscopy, *Membrane Characterization*, Elsevier (2017). Elsevier, https://doi.org/10.1016/B978-0-444-63776-5.00009-7.
21. S. N. Thakur, Chapter 2 Atomic emission spectroscopy, *Laser-Induced Breakdown Spectroscopy*, 2nd Edition, 23, Elsevier (2020). https://doi.org/10.1016/B978-0-12-818829-3.00002-2.
22. M. K. Khan, Q. Y. Wang, and M. E. Fitzpatrick, 1 - Atomic force microscopy (AFM) for materials characterization, *Materials Characterization Using Nondestructive Evaluation (NDE) Methods*, (2016). https://doi.org/10.1016/B978-0-08-100040-3.00001-8.
23. T.-L. Horng, Analyses of Vibration Responses on Nanoscale Processing in a Liquid Using Tapping-Mode Atomic Force Microscopy, *Appl. Surf. Sci.* **256**(1), 311 (2009). https://doi.org/10.1016/j.apsusc.2009.08.021.
24. S. Zhang and C. Wang, Precise analysis of nanoparticle size distribution in TEM image, *Methods Protoc.* **6**(4), 63 (2023). https://doi.org/10.3390/mps6040063.
25. M. T. Al-Helaly and N. A. Al-Tememee, The structural properties of mawsoniteCu$_6$Fe$_2$ S$_8$Sn[CFTS] thin films effected by violet laser irradiation deposited via semi-computerized spray pyrolysis technique, *AIP Conf. Proc.* 2398, 020009 (2022). https://doi.org/10.1063/5.0094321.
26. J. Ou, G. Fang, W. Li, and A. Amirfazli, Wetting transition on textured surfaces: a thermodynamic approach, *J. Phys. Chem.* C. **123**(39), 23976 (2019). https://doi.org/10.1021/acs.jpcc.9b05477.
27. M. A. Saeed, M. Z. Qamar, and Z. Khalid, Two-dimensional MXenes: A route from synthesis to applications in self-powered IoT devices, *Chem. Eng. J.* **490**, 151600 (2024). https://doi.org/10.1016/j.cej.2024.151600.
28. H. Chen, S. Sun, F. Tian, D. Min, L. Liu, and L. Li, Deformation mechanism of Ni-based single crystal superalloy under ultrasonic surface rolling and subsequent thermal exposure, *Surf. Coat. Technol.* 494, part 1, 131369, (2024). https://doi.org/10.1016/j.surfcoat.2024.131369.
29. N. Al-Tememee and S. Al- Ani, the relative quantum efficiency of anthracene solution as a function of light exposure duration, *Iraqi J. Sci.* **50**(Appendix), 19 (2009). https://doi.org/10.24996/ijs.2009.50.Appendix.%25g.

الخواص التركيبية لمركبي $CoFe_2O_4$ و $CoFe_{1.6}Mo_{0.4}O_4$ المحضرين بالطريقة الكيميائية

سرى صلاح مهدي[1] ونذيرة عباس علي[1]
[1]قسم الفيزياء، كلية العلوم، جامعة بغداد، بغداد، العراق

الخلاصة

تناولت هذه الدراسة الخصائص البنيوية لمادتين من الفريت الإسبينلي: فريت الكوبالت (CoFe2O4) وفريت الكوبالت المُطعّم بالموليبدينوم (CoFe2-xMoxO4) (CMFO) حيث x=0.4. وقد نجحت الطريقة الكيميائية في إنتاج جسيمات نانوية مغناطيسية من CoFe2O4 وCoFe1.6Mo0.4O4. واستُخدمت تقنيات المجهر الذري الماسح (AFM) وحيود الأشعة السينية (XRD) والمجهر الإلكتروني الماسح ذو الانبعاث الميداني (FESEM) ومطيافية تشتت طاقة الأشعة السينية (EDX) لدراسة الخصائص البنيوية والمورفولوجية. وأكدت أنماط حيود الأشعة السينية وجود أطوار مكعبة في المركبات. علاوة على ذلك، أشارت نتائج حيود الأشعة السينية (XRD) إلى أن بنية الجسيمات النانوية تُظهر طورًا مختلطًا من CoFe2O4 و CoFe1.6Mo0.4O4، بمتوسط حجم بلوري يتراوح بين 15.166 و 19.638 نانومتر، بما في ذلك تأثير الموليبدينوم. ووفقًا لصور المجهر الإلكتروني الماسح ذي الانبعاث الميداني (FESEM)، كانت جسيمات الفريت المُنتَجة مُتكتلة ودائرية الشكل إلى حد كبير. وأظهرت صورة CoFe2O4 أقطارًا تتراوح بين 67 و 277 نانومترًا، بينما أظهرت صورة CoFe1.6Mo0.4O4 أقطارًا تتراوح بين 59 و 360 نانومترًا. وظهر خط انبعاث للأكسجين (O) وخطوط انبعاث للمعادن (الحديد، والموليبدينوم، والكوبالت) في أطياف حيود الأشعة السينية المشتتة للطاقة (EDX). واستُخدم المجهر الذري الماسح (AFM) لدراسة تضاريس السطح. وتوزعت البنى النانوية ذات الأحجام المتوسطة التي تتراوح بين 123.4 و 94.7 نانومترًا بشكل متجانس في صور المجهر الذري الماسح.

الكلمات المفتاحية: الطريقة الكيميائية، المواد المغناطيسية، الجسيمات النانوية، الفريت، الخصائص الهيكلية.